Hydrodynamics at the moving contact line

Amal K. Giri[1], Paolo Malgaretti[1], Dirk Peschka[2], Marcello Sega[1]

submitted: January 12, 2022

[1] Forschungszentrum Jülich GmbH
Helmholtz Institute Erlangen-Nürnberg for Renewable Energy (IEK-11)
Cauerstr. 1
91058 Erlangen
Germany
E-Mail: a.giri@fz-juelich.de
p.malgaretti@fz-juelich.de
m.sega@fz-juelich.de

[2] Weierstrass Institute
Mohrenstr. 39
10117 Berlin
Germany
E-Mail: dirk.peschka@wias-berlin.de

No. 2911
Berlin 2022

Hydrodynamics at the moving contact line

Amal K. Giri, Paolo Malgaretti, Dirk Peschka, Marcello Sega

Abstract

By removing the smearing effect of capillary waves in molecular dynamics simulations we are able to provide a microscopic picture of the region around the *moving contact line* (MCL) at an unprecedented resolution. On this basis, we show that the continuum character of the velocity field is unaffected by molecular layering down to below the molecular scale. The solution of the continuum Stokes problem with MCL and Navier-slip matches very well the molecular dynamics data and is consistent with a slip-length of 42 Å and small contact line dissipation. This is consistent with observations of the local force balance near the liquid-solid interface.

Introduction

Contact line motion is key to several applications including printable photovoltaics [1], ink-jet printing [2], liquid coating and paint drying processes [3]. One of the main difficulties in modeling the MCL properties is that despite being a mesoscopic quantity, a continuum description fails at describing the region close to it accurately. A naive approach based on the no-slip boundary conditions encounters necessarily a non-integrable stress singularity, raising what is known as the Huh and Scriven paradox [4]. Several mechanisms have been proposed to remove the singularity at the MCL, as discussed in several reviews [5–7], among which, for example, there are the Cox-Voinov law [8, 9], the molecular-kinetic theory [10, 11] and the interface formation theory [12, 13]. Notably, all these approaches rely on the introduction of a microscopic length scale below which the classical hydrodynamics of a homogeneous, incompressible, Newtonian fluid fails. In order to extend the applicability of hydrodyanamics, additional dissipation mechanisms have been suggested, including Navier slip [14] and MCL dissipation [15, 16]. However, the situation is further complicated by the number of physical mechanisms that can contribute to the origin of dissipation at the liquid/solid interface [17, 18], including phonons [19, 20], electronic excitations [21], or charge build-up [22].

Accordingly, a detailed picture is needed to understand what is happening in the MCL region at the molecular scale. Particle-based simulation methods have a long and successful history of contributions to our present understanding of hydrodynamic phenomena. Direct Monte Carlo simulations [23] have provided insightful information for rarified gases, where the simple integration of Newton's law is computationally too expensive, allowing, for example, to investigate deviations from Navier-Stokes equations within the Knudsen layer [24]. MD simulations can deliver a microscopically detailed picture of the MCL [25] and have been successful on many fronts, for example, in evidencing the breakdown of local hydrodynamics [26], providing support for the molecular-kinetic theory both with simple [27] and hydrogen-bonding substrates [28] or investigating the time scale for the liquid/solid tension relaxation [29].

Despite the potential for providing information at the molecular scale, the presence of thermal capillary waves [30] is setting a limit to the resolution one can achieve close to the liquid/vapor interface. Capillary wave theory [31] predicts that spontaneous surface excitations broaden the width of fluid interfaces with a logarithmic divergence that depends on the simulation cell size. For small molecular liquids and typical simulation cells, the fluctuations are larger than the molecular size [30, 32]. Also in this case, a microscopic length scale needs to be introduced, this time to separate long wavelength, hydrodynamic surface oscillations from the intrinsic surface modes. Several computational strategies have been devised to recover the intrinsic structure of fluid interfaces [32–38]. In some of these, including the approach reported here, one first identifies molecules at the phase interface (see Fig. 1), which are then used to build a local coordinate system. In turn, one can use this coordinate system to compute the profiles of chosen observables as a function of the local distance from the interface.
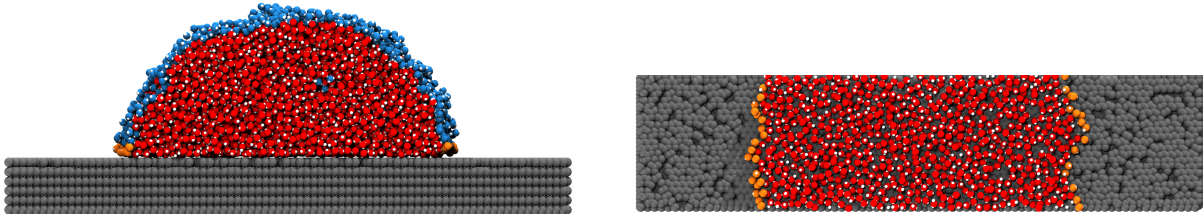
Figure 1: MD simulation snapshot of a cylindrical droplet with 7,332 water molecules in a rectangular cuboid domain of size $L_x \times L_y \times L_z = 198.9 \times 46.8 \times 170\,\text{Å}$ and external acceleration of $\boldsymbol{g} = 5 \times 10^{-3}\,\text{Å/ps}^2$ along the horizontal (x) direction. Red: oxygen atoms; Blue: oxygen atoms at the liquid/vapor interface ; Orange: oxygen atoms at the MCL.
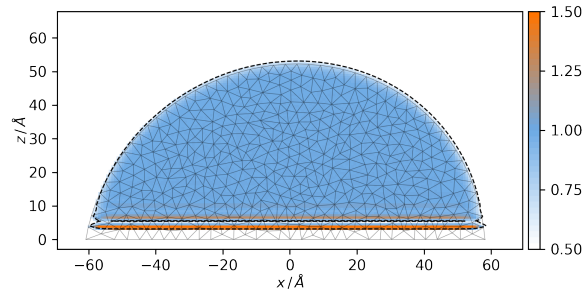

Figure 2: MD density ρ (shading) and its isolevel at $\rho = 0.66 \times \bar{\rho}$ compared to traveling wave solution shape (mesh) of Stokes problem with $\mathrm{Bo} = 0.2414$, $\beta = 0.8$, $\delta = 0$, $\vartheta_e = 97.2°$.

To obtain further insight into the dynamics of the molecules at the MCL, one has to cope with its fluctuations. In this case, however, two interfaces are involved (liquid/vapor and liquid/solid), and one-dimensional intrinsic profiles are not enough to describe the system. Here, we extend the approach of intrinsic profiles to the region around the three-phase contact line by introducing two-dimensional density maps that are functions of the relative position with respect to the liquid/vapor and liquid/solid interfaces, respectively. This procedure allows us to resolve the structure and the flow close to the MCL at an unprecedented resolution.

Compatibility of MD and continuum approach

As detailed in the Appendix, we performed MD simulations of a cylindrical water droplet moving on a rigid substrate under the influence of a constant acceleration parallel to the solid surface.

We modeled the substrate as a rigid, graphite-like structure with defects [39], obtained by removing 10% of randomly selected surface atoms. The presence of defects serves rather well the purpose of providing a friction coefficient thanks to the lateral modulation of the water-surface interaction potential surface. Without the presence of these defects, the droplet would have an almost perfect slip.

The necessary first step to compute intrinsic maps of the droplet's hydrodynamic fields is to identify the surface molecules at the liquid/vapor interface. Here, we use the GITIM algorithm [38] as detailed in the Appendix. In Fig. 3 we show the distribution of these molecules, as well as the associated velocity field (atomic centers of the solid surface are at $z = 0$). The inset shows the neighborhood of the advancing contact line, underlining the structure of the three-phase contact line, which can be identified as the first density peak at $z < 5\,\text{Å}$. As expected, the vanishing velocity (in the co-moving reference frame) at the contact line shows that it moves with the center of mass speed.

Once the surface molecules are identified, we compute the intrinsic map of a generic local observable A as $A(\boldsymbol{\xi}) = \left\langle \sum_i A_i \prod_\alpha \delta\left(\xi_\alpha - |\boldsymbol{r}_i - \boldsymbol{\zeta}_\alpha(\boldsymbol{r}_i)|\right) \right\rangle / N(\boldsymbol{\xi})$. Here, $\boldsymbol{\xi} = (\xi_V, \xi_S)$ are the distances of a point in space from the liquid/vapor and solid surfaces, respectively. The angular brackets indicate a statistical average, the index i labels particles and $\alpha = \{V, S\}$ the instantaneous liquid/vapor and solid surfaces located at $\boldsymbol{\zeta}_V(x, z)$ and $\boldsymbol{\zeta}_S(x, z)$, respectively. One can compute the normalization factor $N(\boldsymbol{\xi})$ by calculating the intrin-
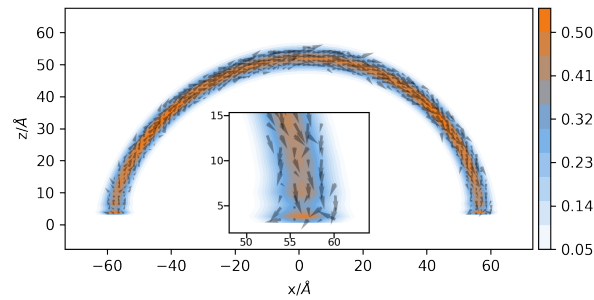
Figure 3: Density and velocity field of the liquid/vapor interfacial layer in the global reference frame. The density and velocity fields are sampled with a resolution of 0.78×0.66 and $1.55\times1.33\,\text{Å}^2$, respectively. The velocity field is scaled such that an arrow of length $1\,\text{Å}$ corresponds to a velocity of $0.01\,\text{Å/ps}$. The inset shows a detail of the advancing contact line region. The atomic centers of the first layer of the substrate are located at $z = 0$.
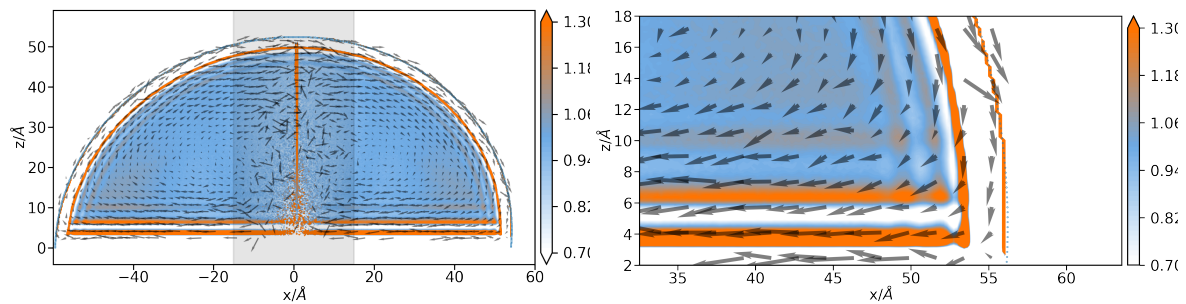

Figure 4: Intrinsic map of the density (normalized to the bulk value, color map) and velocity field in the co-moving reference frame (arrows). The molecules belonging to the liquid/vapor interface, whose distribution is shown in Fig. 3, have zero inherent distance ξ_V and are represented here using the result of an elliptic fit through their average position (small open circles). The density field has resolution $0.22 \times 0.2\,\text{Å}^2$ and is normalized with respect to the bulk density. The velocity field has resolution $1.7 \times 1.6\,\text{Å}^2$, is computed in the droplet co-moving frame, and is scaled such that an arrow of length $1\,\text{Å}$ on the plot corresponds to a velocity of $0.01\,\text{Å/ps}$. (**Left**) shows full droplet and (**right**) details near MCL.

sic density map of uniformly distributed random points within the liquid phase. The two-dimensional correlation function $A(\boldsymbol{\xi})$ is best interpreted if remapped back from the generalized coordinates (ξ_V, ξ_S) to the Cartesian ones using the average location of the interfaces as the origin of the local frame. We report all intrinsic maps using this representation. This approach has the advantage of providing precise information close to the liquid/vapor interface, but it loses accuracy far away from the interface. However, this region is not of concern for the current investigation, which focuses on the neighborhood of the MCL.

The density field reported in Fig. 4 allows us to appreciate the presence of several molecular layers at both the liquid/solid and liquid/vapor interfaces. Moreover, next to the liquid/vapor and solid interfaces, there is a gap region generated by the hard-core repulsion of the interaction potential. As shown in the right panel of Fig. 4, the resolution of the velocity field matches the molecular scale, with bins of size $1.7\times1.6\,\text{Å}^2$), while the density bins are of size $0.22\times0.2\,\text{Å}^2$. We do not observe any trace of an influence of positional correlations on the velocity field, which is a much smoother function of the position than the density.

It is often remarked that linearized hydrodynamics breaks down in simple liquids below scales of few molecular diameters [40, 41]. However, this is true for processes like sound propagation that, at that scale, happen during extremely short times (of the order of a picosecond). In contrast, we obtain the stationary values of the hydrodynamic fields by measuring over time intervals so large that no memory effect can survive.

In Fig. 5 we report the horizontal velocity profile for molecules in the slab $z < 6\,\text{Å}$, computed in the droplet co-moving frame using both the global and intrinsic coordinate systems. The velocity sampled in the global coordinate system extends further than the intrinsic one because of the fluctuations. Both profiles coincide in the region $|x| < 50\,\text{Å}$, showing a steep increase when departing from the droplet center. However, close to the MCL, the velocity profile computed in the global coordinate system flattens out. In contrast, the intrinsic one is compatible over its entire extension with a $v_x \sim 1/x$ power-law slip profile. The profile in the global
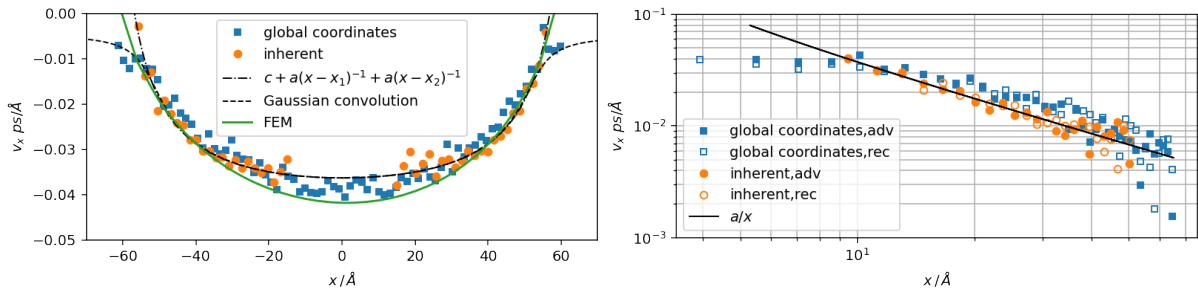
Figure 5: (**Left panel**) Horizontal velocity profiles (squares: global coordinate system, circles: intrinsic profiles) sampled along x at $z = 3 \pm 3\,\text{Å}$. The dot-dashed curve is a fit to a power law $c + a(x - x_1)^{-1} + a(x - x_2)^{-1}$. The dashed line is the convolution of the best-fit power-law with a Gaussian as described in the text. The green curve is the FEM solution evaluated at the interface $z = 0$. (**Right panel**) double logarithmic scale, same data as in the left panel but symmetrized along the vertical axis and shifted so that the fitting constants c and x_1 are zero.
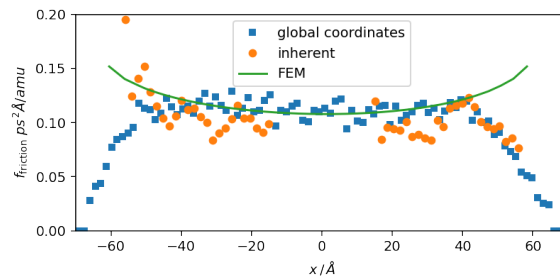

Figure 6: Profile of the friction surface density computed from the MD data in the global (squares) and intrinsic (circles) coordinate systems. The green curve is the FEM solution evaluated at the interface $z = 0$.

coordinate system can be very well described in the spirit of the capillary wave theory by using quantities $\widetilde{A}(x) = \int_{-\infty}^{\infty} G(y)\rho(x - y)dy$ convoluted with the Gaussian distribution $G(x) \sim \exp[-x^2/(2\sigma^2)]$ of the interface fluctuations, so that $v_x = \widetilde{p}_x/\widetilde{\rho}$.

In the left panel of Fig. 5 we report as a dashed-line the velocity profile obtained by applying this convolution procedure to the best fit intrinsic velocity profile $v_x \sim 1/x$ and a step-like density profile, using the interfacial layer width $\sigma = 2.5\text{Å}$. The resulting profile reproduces very well the flattening of the profile in the region close to the MCL. The $1/x$ profile in the intrinsic coordinate system and the departure from it in the global one are more evident in the double logarithmic scale, reported in the right panel of Fig. 5, where we have symmetrized the profile around its minimum and shifted it vertically and horizontally by the fitting constants x_1 and c.

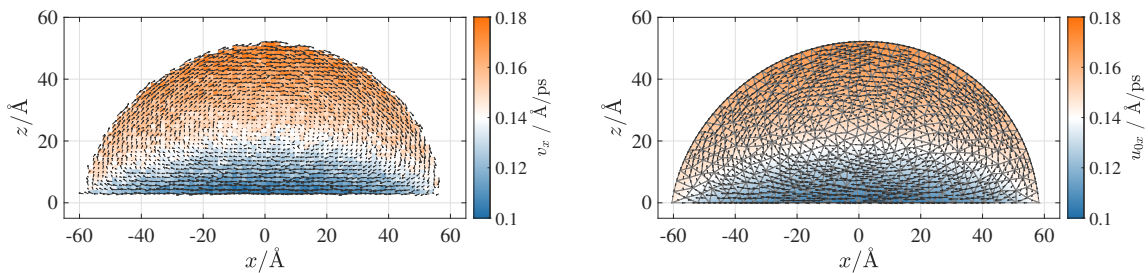Figure 7: (**Left**) Averaged MD velocity profile $\boldsymbol{v} = (v_x, v_z)$ (shown for $\rho > 0.66\bar{\rho}$) compared to (**right**) optimal Stokes velocity profile $\boldsymbol{u}_0 = (u_{0x}, u_{0z})$ for $\beta = 1.3$ (slip-length $b = 42\text{Å}$) and $\gamma = 0$, $\text{Bo} = 0.2414$ and $\vartheta_e = 97.2°$ in a comoving frame (vectors) and absolute horizontal velocity (shading).

Direct comparison of MD and FE Stokes problem

In the past, gravity-driven sliding droplets have been modeled in the continuum approximation using full hydrodynamic models with diffuse or sharp interfaces [42, 43] and by reduced thin-film models [44, 45]. In experiments, cornered droplets have been observed and explained by the structure of the local flow near the rear tip [46]. In particular the dynamic law for the MCL proposed in [47] has been adopted in full hydrodynamic descriptions and reduced variational models [43, 48, 49].

We compare our MD simulations with a full hydrodynamic continuum model for the MCL, where we solve a Stokes problem for an incompressible viscous Newtonian fluid (Re=0) featuring a free interface with capillary forces, which is driven by a constant acceleration g, and contains dissipative processes due to viscous friction, Navier-slip $\beta u_x = \mu \partial_z u_x$ and with a dynamic contact line that has the normal velocity $\nu_x \cdot u_x = \gamma/\delta(\cos\theta_\mathrm{e} - \cos\theta)$, cf. [47]. For this purpose, we discretize the corresponding system of partial differential equations using the isoparametric $P_2 - P_1$ finite elements method (FEM) with ALE mesh motion strategy as in [43, 49]. We report details on the model, nondimensionalization, and general behavior of the solutions in the Appendix.

In general, notice that increasing the friction coefficient β in the Navier-slip condition enhances the asymmetry of the droplet, and the flow profile becomes more inhomogeneous, that is, $\partial_z u_x$ increases while the average velocity of the droplet decreases. In contrast, the influence of the friction parameter δ on the solution is mainly visible in the average velocity and the asymmetry of the drop shape (see Fig. 10).

We compare the velocity of $2d$ traveling-wave solutions $\boldsymbol{u}(t, \boldsymbol{r}) = \boldsymbol{u}_0(x - v_0 t, z)$ with the averaged velocity from the MD simulation $\boldsymbol{v} = (v_x, v_z)$. For given acceleration g, droplet size L, viscosity μ, and equilibrium contact angle ϑ_e, we solve the Stokes problem for different β and δ and then compare this solution to MD data by computing the root mean square deviation (rmsd) Δ as

$$\Delta^2 = \int_{\Omega_0} \rho(\boldsymbol{r}) |\boldsymbol{u}_0(\boldsymbol{r}) - \boldsymbol{v}(\boldsymbol{r})|^2 \, \mathrm{d}\boldsymbol{r} \Big/ \int_\Omega \rho(\boldsymbol{r}) \, \mathrm{d}\boldsymbol{r} \tag{1}$$

in a comoving frame $\Omega_0 = \Omega - (v_0, 0)t$. In the Appendix we report (Fig. 11) the rmsd curves, from which one can clearly see that there are locally optimal solutions in the range $0 < \beta < \beta_\mathrm{max} \sim 1.3$ for each $\delta = \{0, 0.1, 0.2, 0.4\}$. While the lowest rmsd is the one for $\delta = 0$, due to the fluctuations in the MD flow field, see left panel of Fig. 7, and due to the relatively slight deviation of the droplet from its equilibrium shape, (see Fig. 12 in the Appendix), the precise determination of δ is prone to errors. The possible optimal β decreases from $\beta = \beta_\mathrm{max}$ for $\delta = 0$ for increasing δ until it hits $\beta = 0$ for a finite upper value of $\delta = \delta_\mathrm{max}$. Nevertheless, based on the symmetry of the solution, the value should be confined within $0 < \delta < 0.1$. This prediction is compatible with the rmsd-based fit of the velocity fields and the low asymmetry of the MD droplet shape. Exemplary sliding Stokes droplets in the Appendix in Fig. 10 show which amount of contact line friction would be required to generate a certain asymmetry (or advancing and receding angle).

The water molecules are subjected to a friction force that, at steady state, balances g and is defined as the horizontal component of the force density $f_{\Gamma,x}(x, z)$ acting from the substrate on water molecules. Even though long-range corrections for van der Waals interactions are in place, the friction becomes negligible at elevations larger than $z \simeq 10\text{Å}$ and is acting in practice on the first layer of water molecules at the substrate. Therefore, we can define a friction force per unit area as

$$F_\Gamma(x) = \int_0^\infty f_{\Gamma,x}(x, z) dz. \tag{2}$$

This force is the counterpart of the surface friction that in sharp interface models like the present FEM can be calculated from the stress $\boldsymbol{t} \cdot \boldsymbol{\sigma\nu} \equiv -\mu_\Gamma \boldsymbol{t} \cdot \boldsymbol{u}$ at the solid boundary.

Fig. 6 shows the friction surface density F_Γ obtained from the MD trajectories and compared to the FEM results. Far from the droplet edges, both methods are in excellent agreement. However, close to the advancing and receding MCL, the friction force behaves qualitatively differently. This mismatch is in contrast to the overall good match of the slip velocity profile Fig. 5. Therefore, even though the Navier boundary condition is a good effective

model in reproducing the slip velocity, the same is not true concerning the friction force. Remarkably, even in the present case where the substrate is particularly smooth, and the optimal FEM solution is compatible with zero contact line dissipation, we observe a significant deviation of the friction force from the one emerging from the Navier condition. Therefore, we expect larger defects or soft substrates to enhance this deviation substantially.

Conclusion

We introduced improved averages of MD simulations that remove the smearing effect due to capillary waves near the interfaces. This procedure allows us to compute averages with higher accuracy than the standard approaches and thereby, in particular, improve averages near the interface. From this, we can conclude that the typical hydrodynamic behavior of the velocity field is valid down to the molecular scale. From a direct comparison of averages with FEM solutions of an incompressible Stokes problem with MCL and Navier-slip condition, we determine the slip-length to be 42 Å and find little contact line dissipation. Future studies will extend this approach to larger droplets and stronger contact line dissipation.

A   Appendix

A.1   Molecular dynamics simulation and intrinsic analysis details

We produced the trajectories using the GROMACS simulation package, release 2019.4 [50] employing the SPC/E interaction potential [51] and the geometrical and interaction parameters reported in Ref. [39] for the substrate (six layers). We integrated the equations of motion in the canonical ensemble for $0.5\,\mu s$ using the leapfrog algorithm (2 fs integration timestep Δt) and a Nosé-Hoover [52, 53] thermostat with 1 ps time constant, modified to couple only to the direction orthogonal to both the surface normal and the external force direction [26], keeping in mind that this introduces a bias in the surface energies [54]. We constrain the geometry of water molecules [55] and keep the substrate atoms fixed. We compute the long-range part of Coulomb and dispersion interactions using the smooth version of the particle-mesh Ewald method [56] with a grid spacing of 1.2 Å, fourth-order polynomial interpolation scheme, short-range cutoff of 12 Å, metallic boundary conditions, and a relative interaction strength at the cutoff of 10^{-5} and 10^{-3} for the Coulomb and dispersion terms, respectively. We simulate 7332 water molecules in a rectangular simulation box of size $198.9 \times 46.8 \times 170\,\text{Å}^3$ in a cylindrical droplet configuration. Periodic boundary conditions apply so that there is an approximate translational invariance along the y axis. The external acceleration of $5 \times 10^{-3}\text{Å/ps}^2$ acts along the x axis, while the surface normal points along z. We store positions, velocities, and forces to disk every ps for postprocessing with the MDAnalysis [57] and Pytim [58] analysis packages. Even though the vapor pressure is practically zero, we exclude rare gas molecules from the interfacial analysis by defining the droplet as the largest cluster of molecules having a neighbor within 3.5 Å, the first minimum of the oxygen pair correlation function in the bulk. Surface molecules are identified using the GITIM algorithm [38, 58] with a probe sphere radius of 2 Å. We compute all hydrodynamic fields on a molecular basis, with the velocity one calculated as the ratio of the local momentum to the local mass. Since the data reported are always correlations with positions (the center of mass of the droplet in the standard case, the surface atoms in the intrinsic case), it is critical to evaluate physical quantities simultaneously. Notably, GROMACS is storing velocities at the previous half-step, and obtaining the full step value, we add to each atom the correction $\Delta t f_i/2$, where f_i/m_i is the acceleration of the particle of mass m_i at full step. Failure to do so introduces severe unphysical effects, particularly evident at rigid boundaries. To compute the normalization factor $N(\boldsymbol{\xi})$ we generate about 7×10^4 random points for each analyzed frame. To remap the intrinsic maps to the Cartesian coordinates, we use as a reference for the two surfaces the location of the uppermost layer of the solid substrate (located at $z = 0$ and the locus of the ellipse that fits best the average positions (obtained by binning at constant angular intervals with respect to the center of droplet base) of the liquid/vapor surface molecules.

A.2 Dimensionless numbers

The dimensionless numbers characterizing the problem are the

$$
\begin{aligned}
\text{Reynolds number} \quad & \mathrm{Re} = \frac{2Rv_{cm}}{\mu} \simeq 0.2, \\
\text{Mach number} \quad & \mathrm{Ma} = \frac{v_{cm}}{c_s} \simeq 0.01, \\
\text{capillary number} \quad & \mathrm{Ca} = \frac{\mu v_{cm}}{\gamma} \simeq 0.2, \\
\text{Bond number} \quad & \mathrm{Bo} = \frac{\rho R^2 g}{\gamma} = 0.2414,
\end{aligned}
$$

where μ=0.72 mPa s is the dynamic viscosity, c_s=1460 m/s [59] the speed of sound, γ=61.8 mN/m [60] the surface tension, ρ=996.8 kg m/s^2 [60] the mass density, v_{cm}=1.47Å/ps the velocity of the center of mass and $g = 5 \times 10^{-3}$Å/ps^2 the acceleration imposed on the fluid molecules. The best fit of an arc of a circle through the surface atoms yields the droplet equilibrium contact angle $\vartheta_e = 97.2°$ and an effective radius $R = 54.8$Å. For details about the nondimensionalization of the corresponding continuum problem, see Appendix A.4.

A.3 Weak formulation for Stokes free boundary problem.

In the paper we consider, as a mesoscopic problem, the evolution of an incompressible liquid drop following the Stokes free boundary problem

$$
\begin{aligned}
-\nabla \cdot \boldsymbol{\sigma} = \boldsymbol{f} \quad \text{and} \quad \nabla \cdot \boldsymbol{u} = 0 & \qquad \text{conservation of momentum and mass in } \Omega(t) , && \text{(3a)} \\
\boldsymbol{t} \cdot \boldsymbol{\sigma}\boldsymbol{\nu} = -\mu_\Gamma \boldsymbol{t} \cdot \boldsymbol{u} & \qquad \text{Navier-slip on } \Gamma_{\mathrm{s}\ell}(t) , && \text{(3b)} \\
\boldsymbol{\sigma}\boldsymbol{\nu} = \gamma \kappa \boldsymbol{\nu} & \qquad \text{capillary forces on } \Gamma_\ell(t) , && \text{(3c)} \\
\mu_\Lambda \dot{\mathrm{x}} = f_\Lambda & \qquad \text{dynamic contact angle on } \Lambda(t) , && \text{(3d)}
\end{aligned}
$$

where the domains are time-dependent: Ω is the fluid domain, $\Gamma_{\mathrm{s}\ell}$ is the fluid-substrate interface, Γ_ℓ is the fluid-air interface, $\Lambda = \partial\Gamma_{\mathrm{s}\ell}$ is the contact line, and $\boldsymbol{t}$ and $\boldsymbol{\nu}$ are corresponding tangential and normal vectors. In this problem $\boldsymbol{f} = \rho\boldsymbol{g}$ is a given bulk force, f_Λ is the x-component of the uncompensated Young force $\boldsymbol{f}_\Lambda = \gamma\boldsymbol{\nu}_{\Gamma_\ell} + \gamma_{\mathrm{s}\ell}\boldsymbol{\nu}_{\Gamma_{\mathrm{s}\ell}} = (f_\Lambda, f_{\Lambda z})$, the Cauchy stress of the Newtonian fluid is $\boldsymbol{\sigma} = -p\mathbb{I} + \mu(\nabla\boldsymbol{u} + \nabla\boldsymbol{u}^t)$ with bulk viscosity μ, μ_Γ encodes the Navier-slip condition, μ_Λ encodes the dynamic contact angle, γ_i are the surface tensions and κ the mean curvature of the fluid-air interface. The Stokes free boundary problem is based a Lagrangian formulation with displacements, which is converted into a Eulerian formulation for $\boldsymbol{r} = (x, z) \in \Omega(t) \subset \mathbb{R}^d$ with the free energy

$$
\mathscr{F}\big(\boldsymbol{q}(t)\big) = \int_{\Omega(t)} \rho\boldsymbol{g} \cdot \boldsymbol{r} \, \mathrm{d}x\,\mathrm{d}z + \gamma \int_{\Gamma_\ell(t)} \mathrm{d}s + \gamma_{\mathrm{s}\ell} \int_{\Gamma_{\mathrm{s}\ell}(t)} \mathrm{d}s,
$$

where the state $\boldsymbol{q}$ basically contains the deformed domain shapes. In the transient problem we use bilinear forms

$$
a(\boldsymbol{u}, \boldsymbol{v}) = \int_{\Omega(t)} 2\mu\mathbb{D}(\boldsymbol{u}) : \mathbb{D}(\boldsymbol{v}) \, \mathrm{d}x\,\mathrm{d}z + \int_{\Gamma_{\mathrm{s}\ell}(t)} \mu_\Gamma u \cdot v \, \mathrm{d}x + \int_{\Lambda(t)} \mu_\Lambda \, u \cdot v \, \mathrm{d}\ell, \tag{4a}
$$

$$
b(\boldsymbol{u}, p) = \int_{\Omega(t)} p\nabla \cdot \boldsymbol{u} \, \mathrm{d}x\,\mathrm{d}z, \tag{4b}
$$

and which the tangential derivative $\nabla_\parallel$, the shape/Fréchet derivative of the energy can be written

$$
\langle \mathrm{D}\mathscr{F}(\boldsymbol{q}), \boldsymbol{v} \rangle = \int_{\Omega(t)} \rho\boldsymbol{g} \cdot \boldsymbol{v} \, \mathrm{d}x\,\mathrm{d}z + \gamma \int_{\Gamma_\ell(t)} \nabla_\parallel \mathrm{id} \cdot \nabla_\parallel \boldsymbol{v} \, \mathrm{d}s + \gamma_{\mathrm{s}\ell} \int_{\Gamma_{\mathrm{s}\ell}(t)} \nabla_\parallel \mathrm{id} \cdot \nabla_\parallel \boldsymbol{v} \, \mathrm{d}s. \tag{4c}
$$

Based on these bilinear forms, in the emerging saddle-point problem for the Stokes problem we seek the velocity field $\boldsymbol{u}(t) = (u, u_z) : \Omega(t) \to \mathbb{R}^d$ and the pressure $p(t) : \Omega(t) \to \mathbb{R}$ such that

$$b(\boldsymbol{u}(t), q) = 0, \tag{4d}$$

$$b(\boldsymbol{v}, p(t)) + a(\boldsymbol{u}(t), \boldsymbol{v}) = -\langle \mathrm{D}\mathscr{F}(\boldsymbol{q}(t)), \boldsymbol{v} \rangle, \tag{4e}$$

for all test functions $\boldsymbol{v} = (v, v_z)$ and q. With the resulting velocity fields $\boldsymbol{u}(t)$, the domain (mesh) is deformed by mapping (the vertices) $\boldsymbol{r} \mapsto \boldsymbol{r} + \tau \boldsymbol{w}$ using the kinematic condition $(\boldsymbol{u} - \boldsymbol{w}) \cdot \boldsymbol{\nu} = 0$ on $\partial\Omega(t)$, which allows to choose a suitable extension $\boldsymbol{w} : \Omega \to \mathbb{R}^d$, i.e., harmonic extension, that maintains the mesh quality. This weak formulation (4) is implemented using isoparametric Taylor-Hood $\boldsymbol{P}_2/P_1$ finite elements, i.e.,

$$\boldsymbol{u}(t, \boldsymbol{\chi}(\bar{\boldsymbol{r}})) = \sum_{n=1}^{\dim \boldsymbol{V}_h^2} u_h^n(t) \bar{\boldsymbol{\varphi}}_n(\bar{\boldsymbol{r}}), \qquad p(t, \boldsymbol{\chi}(\bar{\boldsymbol{r}})) = \sum_{n=1}^{\dim V_h^1} p_h^n(t) \bar{\psi}_n(\bar{\boldsymbol{r}}), \qquad \boldsymbol{\chi}(t, \bar{\boldsymbol{r}}) = \sum_{n=1}^{\dim \boldsymbol{V}_h^2} \boldsymbol{\chi}_h^n(t) \bar{\boldsymbol{\varphi}}_n(\bar{\boldsymbol{r}}),$$

where the functions $\boldsymbol{u}(t) : \Omega \to \mathbb{R}^d$ and $\boldsymbol{p}(t) : \Omega \to \mathbb{R}$ on a domain Ω with curved boundaries are approximated using basis functions $\bar{\boldsymbol{\varphi}}_n \in \boldsymbol{V}_h^2$ and $\bar{\psi}_n \in V_h^1$ defined on a domain $\bar{\Omega}$ with polygonal boundaries using a $\boldsymbol{P}_2$ map $\bar{\boldsymbol{\chi}} : \bar{\Omega} \to \Omega(t)$ and a corresponding triangulation $\{\mathscr{T}_h\}_{h>0}$ with

$$\boldsymbol{V}_h^k = \{\boldsymbol{v} \in C^1(\bar{\Omega}, \mathbb{R}^d) : \boldsymbol{v}|_T \in P_k(T, \mathbb{R}^d), T \in \mathscr{T}_h\}, \qquad V_h^k = \{v \in C^1(\bar{\Omega}) : v|_T \in P_k(T, \mathbb{R}), T \in \mathscr{T}_h\}.$$

$P_k(T, V)$ being V-valued polynomials on T. Then the domain motion is facilitated by the ALE evolution of $\boldsymbol{\chi}_h^n(t)$, i.e., $\chi_h^n(t + \tau) = \chi_h^n(t) + \tau w_h^n$, where $\boldsymbol{w} \in \boldsymbol{V}_h^k$ solves the ALE problem

$$(\boldsymbol{w}, \lambda) = \underset{(\hat{\boldsymbol{w}}, \hat{\lambda})}{\operatorname{argmin}} \int_{\Omega(t)} \tfrac{1}{2} |\nabla \hat{\boldsymbol{w}}|^2 \, \mathrm{d}x \, \mathrm{d}z + \int_{\partial\Omega} \hat{\lambda} (\hat{\boldsymbol{v}} - \boldsymbol{u}) \cdot \boldsymbol{\nu} \, \mathrm{d}s, \tag{5}$$

and the kinematic condition is enforced using a Lagrange multiplier $\lambda : \partial\Omega \to \mathbb{R}$ on the boundary.

A.4 Nondimensionalization of the Stokes problem and initial data.

We rescale (4) by introducing dimensional scales for length, velocity and time

$$\boldsymbol{r} = (x, z) = (R\,\tilde{x}, R\,\tilde{z}), \qquad \boldsymbol{u} = U\tilde{\boldsymbol{u}}, \qquad t = \frac{R}{U}\tilde{t},$$

so that the bilinear form can be nondimensionalized

$$\tilde{a}(\tilde{\boldsymbol{u}}, \tilde{\boldsymbol{v}}) = \frac{a(\boldsymbol{u}, \boldsymbol{v})}{\mu R^{d-2} U^2} = \int_{\tilde{\Omega}} 2\mathbb{D}(\tilde{\boldsymbol{u}}) : \mathbb{D}(\tilde{\boldsymbol{v}}) \, \mathrm{d}\tilde{x} \, \mathrm{d}\tilde{z} + \int_{\tilde{\Gamma}_{s\ell}} \frac{\mu_\Gamma R}{\mu} \tilde{u} \cdot \tilde{v} \, \mathrm{d}\tilde{s} + \int_{\tilde{\Lambda}} \frac{\mu_\Lambda}{\mu} \tilde{u} \cdot \tilde{v} \, \mathrm{d}\tilde{\ell} \tag{6}$$

where we introduce the new nondimensional parameters

$$\beta = \frac{\mu_\Gamma R}{\mu}, \qquad \delta = \frac{\mu_\Lambda}{\mu}, \tag{7}$$

where we have the relation to the slip-length $b = R/\beta$ and δ encodes the ratio of friction at the contact line relative to bulk viscosity. By balancing viscous and capillary forces via $U = \gamma/\mu$, we rescale the driving force to become

$$\langle \mathrm{D}\tilde{\mathscr{F}}(\tilde{\boldsymbol{q}}), \tilde{\boldsymbol{v}} \rangle = \frac{1}{\mu R^{d-2} U^2} \langle \mathrm{D}\mathscr{F}(\boldsymbol{q}), \boldsymbol{v} \rangle$$

$$= \int_{\tilde{\Omega}} \frac{\rho |\boldsymbol{g}| R^2}{\mu U} \frac{\boldsymbol{g}}{|\boldsymbol{g}|} \cdot \tilde{\boldsymbol{v}} \, \mathrm{d}\tilde{x} \, \mathrm{d}\tilde{z} + \int_{\tilde{\Gamma}_\ell} \nabla_\parallel \mathrm{id} \cdot \nabla_\parallel \tilde{\boldsymbol{v}} \, \mathrm{d}\tilde{s} + \frac{\gamma_{s\ell}}{\gamma} \int_{\tilde{\Gamma}_{s\ell}} \nabla_\parallel \mathrm{id} \cdot \nabla_\parallel \tilde{\boldsymbol{v}} \, \mathrm{d}\tilde{s}. \tag{8}$$
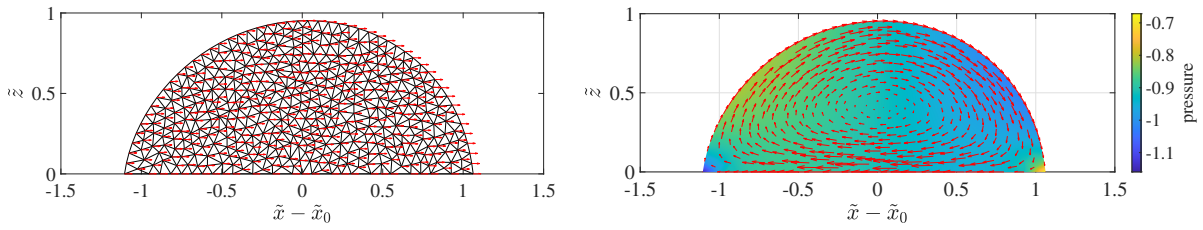
Figure 8: Exemplary traveling wave solution with $\beta = 0.2$, $\delta = 0$, $\mathrm{Bo} = 0.2414$, $R = 54.799\,\text{Å}$, $U = 0.8477\,\text{Å/ps}$ and $\vartheta_e = 180° - 82.8°$ showing (**left**) solution with triangular mesh (black) and velocity field $\boldsymbol{u}_0$ (red arrows) and (**right**) pressure p_0 (shading) and comoving velocity fields $\boldsymbol{u}_0 - \boldsymbol{v}_0$ (red arrows). Solution is translated to origin using the center of mass $\tilde{x}_0 = V^{-1} \int \tilde{x}\,\mathrm{d}\tilde{x}\,\mathrm{d}\tilde{z}$.

where we usually set $\boldsymbol{g}/|\boldsymbol{g}| = \boldsymbol{e}_x$ and introduce the two additional nondimensional parameters

$$\mathrm{Bo} = \frac{\rho|\boldsymbol{g}|R^2}{\mu U} \equiv \frac{\rho|\boldsymbol{g}|R^2}{\gamma}, \qquad \cos\vartheta_e = -\frac{\gamma_{s\ell}}{\gamma}, \tag{9}$$

the first being the Bond number and the latter encoding the equilibrium contact angle ϑ_e. Note that only within the interval $-1 < \frac{\gamma_{s\ell}}{\gamma} < 1$ equilibrium droplets are possible. This results in the nondimensional weak formulation

$$\tilde{b}(\tilde{\boldsymbol{u}}, \tilde{r}) = 0\,,$$
$$\tilde{b}(\tilde{\boldsymbol{v}}, \tilde{p}) + \tilde{a}(\tilde{\boldsymbol{u}}, \tilde{\boldsymbol{v}}) = -\langle \mathrm{D}\tilde{\mathscr{F}}(\tilde{\boldsymbol{q}}), \tilde{\boldsymbol{v}}\rangle\,,$$

where $\tilde{b}$ remains basically unchanged since arbitrary constants can be absorbed into the Lagrange multiplier.

In the numerical simulation we seek traveling wave solutions, i.e., solutions which for $t \to \infty$ behave as

$$\tilde{\Omega}(t) = \Omega_0 + \boldsymbol{v}_0 t, \qquad \boldsymbol{u}(t, \boldsymbol{r}) = \boldsymbol{u}_0(\boldsymbol{r} - \boldsymbol{v}_0 t), \qquad p(t, \boldsymbol{r}) = p_0(\boldsymbol{r} - \boldsymbol{v}_0 t), \tag{10}$$

for some constant droplet speed $\boldsymbol{v}_0 = (v_0, 0) \in \mathbb{R}^d$ with flow field $\boldsymbol{u}_0 : \Omega_0 \to \mathbb{R}^d$ and pressure $p_0 : \Omega_0 \to \mathbb{R}$. For the initial domain shape at $t = 0$ we use a unit semidisc

$$\tilde{\Omega}(t=0) = B_1(0) \cap \mathbb{R}_+ = \{\tilde{\boldsymbol{r}} = (\tilde{x}, \tilde{z}) \in \mathbb{R} \times \mathbb{R}_+ : \tilde{x}^2 + \tilde{z}^2 < 1\}, \tag{11}$$

and adjust the scaling R to match the initial mass/volume of the MD simulations, see Fig. 8. We chose Ω_0 so that the center of mass alignes with zero, i.e., $\int_{\Omega_0} x\,\mathrm{d}x\,\mathrm{d}z = 0$.

A.5   Determination of initial state and equilibrium contact angle.

In order to obtain the initial scale of the droplet for the Stokes simulation, we have two equivalent options: Adjust the volume of the initial mesh to the total volume based on the molecular volume $V_{H_2O} = 30\,\text{Å}^3$ or using the molecular mass $M_{H_2O} = 18\,\text{g\,mol}^{-1}$. Since the MD simulation domain has a depth of $D = 46.8\,\text{Å}$ and the simulation uses 7332 molecules, this gives a cross sectional area of $A = 7332 \times V_{H_2O}/D = 4700\,\text{Å}^2$. Alternatively, the MD droplet has a mass of $M = 7332 \times M_{H_2O}/N_A = 2.192 \times 10^{-22}\,\text{kg}$, which at an equilibrium density of $\rho = 996.8\,\text{kg\,m}^{-3}$ gives the consistent sectional area $A = MD^{-1}\rho^{-1}$. This cross sectional area is contained in a cylindrical cap of the same volume, if we define the interface at the density level $\rho = 0.66 \times \bar{\rho}$ of the bulk value $\bar{\rho}$ and fit the part for $z > 7\text{Å}$ to a cap, as shown in Fig. 9.
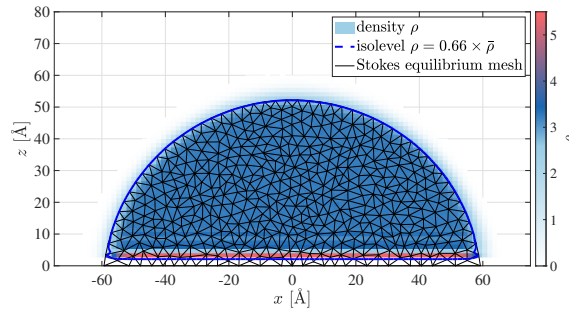
Figure 9: MD density ρ and isolevel at $\rho = 0.66 \times \bar{\rho}$ compared to mesh of the Stokes solver at equilibrium with $\vartheta_e = 97.2°$.

From this fit to a spherical cap we deduce the nondimensional parameters $R = 54.8\text{Å}$, $\vartheta_e = 97.2°$, $\text{Bo} = 0.2414$, as input data for the Stokes free boundary problem. Note that the contact angle is the outer angle.

A.6 Discussion of Stokes solution with different β and δ.

In the nondimensionalized problem (6) the viscosity is scaled to unity and includes only the nondimensional parameters relating to friction at the liquid-solid interface $\beta = R/b$, where b is the corresponding slip length, and friction at the contact line δ. Here we discuss the qualitative impact that different choices of $\beta \in \{10^{-1}, 1, 4\}$ and $\delta \in \{0, 1, 10\}$ have on the droplets flow field $\boldsymbol{u}_0(\boldsymbol{r})$ for $\text{Bo} = 1/2$ and $\vartheta_e = 90°$. Note that $\delta = \beta = 0$ is excluded, since without inertial the flow field does not become stationary. For simplicity, we exclude this case from our considerations but choose either β or δ positive.
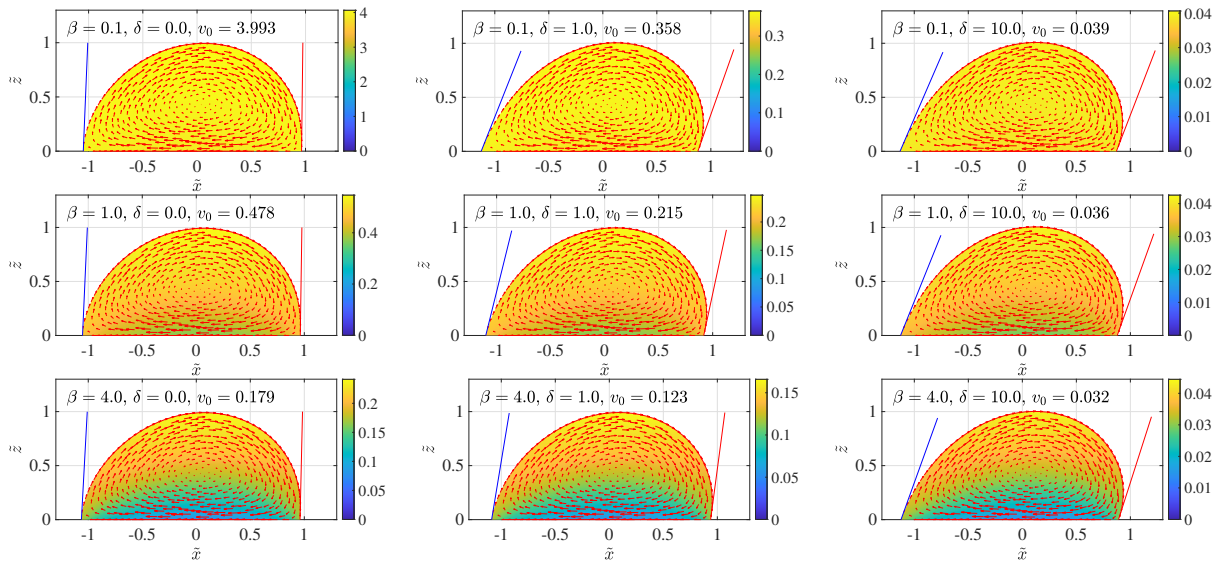

Figure 10: Traveling wave solutions of the Stokes problem for different parameters $\beta \in \{0.1, 1, 4\}$ and $\delta \in \{0, 1, 10\}$. The comoving flow field $\boldsymbol{u}_0 - \boldsymbol{v}_0$ is shown in red vectors, the x-component u_0 of $\boldsymbol{u}_0 = (u_0, u_{z0})$ is shown using the colored shading and the advancing and receding contact angle are shown using red and blue lines. While in all cases $\boldsymbol{u}_0 - \boldsymbol{v}_0$ shows a rolling motion, the main impact of β is to introduce gradients in the absolute velocity, observable in the different shadings of u_0. The main impact of δ is to steer the magnitude of the dynamic contact angle, where for $\delta = 0$ except for small numerical dissipation $\vartheta_e = 90°$. In each case the velocity v_0 decreases when additional dissipation is introduced, i.e., if either β or δ increase. For $\delta = 10$ the velocity depends only weakly on β and is almost entirely controlled by the contact line dissipation.
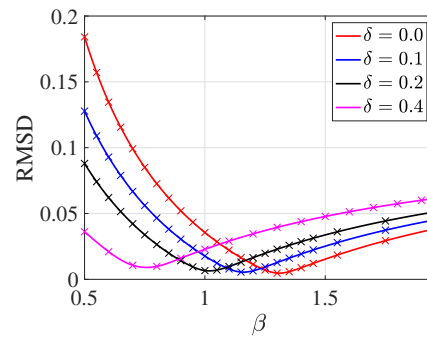
Figure 11: Root-mean-square deviation RMSD of Stokes and MD velocities computed by Eq. (1).
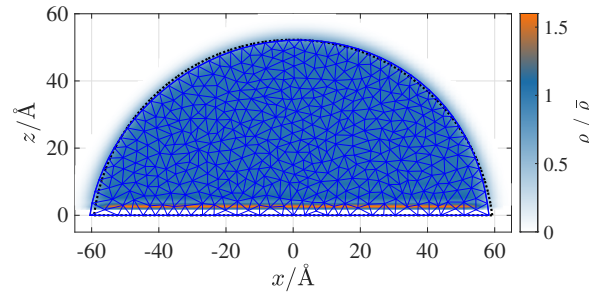

Figure 12: Comparison of normalized MD density $\rho/\bar{\rho}$ with shape of optimal Stokes droplet ($\beta = 1.3$, $\delta = 0$, blue outline and mesh) and equilibrium shape ($\mathrm{Bo} = 0$, dotted).

References

[1] J. J. Berry, J. van de Lagemaat, M. M. Al-Jassim, S. Kurtz, Y. Yan, and K. Zhu, "Perovskite photovoltaics: The path to a printable terawatt-scale technology," *ACS Energy Lett.*, vol. 2, no. 11, pp. 2540–2544, 2017.

[2] M. Singh, H. M. Haverinen, P. Dhagat, and G. E. Jabbour, "Inkjet printing—process and its applications," *Adv. Mater.*, vol. 22, no. 6, pp. 673–685, 2010.

[3] R. D. Deegan, O. Bakajin, T. F. Dupont, G. Huber, S. R. Nagel, and T. A. Witten, "Contact line deposits in an evaporating drop," *Phys. Rev. E*, vol. 62, no. 1, p. 756, 2000.

[4] C. Huh and L. Scriven, "Hydrodynamic model of steady movement of a solid/liquid/fluid contact line," *J. Colloid Interface Sci.*, vol. 35, pp. 85–101, Jan. 1971.

[5] C. Neto, D. R. Evans, E. Bonaccurso, H.-J. Butt, and V. S. J. Craig, "Boundary slip in Newtonian liquids: A review of experimental studies," *Rep. Prog. Phys.*, vol. 68, pp. 2859–2897, Dec. 2005.

[6] D. Bonn, J. Eggers, J. Indekeu, J. Meunier, and E. Rolley, "Wetting and spreading," *Rev. Mod. Phys.*, vol. 81, pp. 739–805, May 2009.

[7] J. H. Snoeijer and B. Andreotti, "Moving Contact Lines: Scales, Regimes, and Dynamical Transitions," *Annu. Rev. Fluid Mech.*, vol. 45, pp. 269–292, Jan. 2013.

[8] O. V. Voinov, "Hydrodynamics of wetting," *Fluid Dyn.*, vol. 11, no. 5, pp. 714–721, 1976.

[9] R. G. Cox, "The dynamics of the spreading of liquids on a solid surface. Part 1. Viscous flow," *J. Fluid Mech.*, vol. 168, pp. 169–194, 1986.

[10] T. Blake and J. Haynes, "Kinetics of liquidliquid displacement," *J. Colloid Interface Sci.*, vol. 30, pp. 421–423, July 1969.

[11] T. Blake and J. De Coninck, "The influence of solid–liquid interactions on dynamic wetting," *Adv. Colloid Interface Sci.*, vol. 96, pp. 21–36, Feb. 2002.

[12] Y. D. Shikhmurzaev, "Moving contact lines in liquid/liquid/solid systems," *J. Fluid Mech.*, vol. 334, pp. 211–249, 1997.

[13] Y. D. Shikhmurzaev, "The moving contact line on a smooth solid surface," *Int. J. Multiph. Flow*, vol. 19, no. 4, pp. 589–610, 1993.

[14] E. Lauga, M. Brenner, and H. Stone, *Microfluidics: The no-slip boundary condition*, pp. 1219–1240. Springer Handbooks, Springer, 2007.

[15] M. J. De Ruijter, J. De Coninck, and G. Oshanin, "Droplet spreading: Partial wetting regime revisited," *Langmuir*, vol. 15, no. 6, pp. 2209–2216, 1999.

[16] P. G. de Gennes, "Wetting: Statics and dynamics," *Rev. Mod. Phys.*, vol. 57, pp. 827–863, July 1985.

[17] M. H. Müser, M. Urbakh, and M. O. Robbins, "Statistical Mechanics of Static and Low-Velocity Kinetic Friction," in *Advances in Chemical Physics* (I. Prigogine and S. A. Rice, eds.), pp. 187–272, Hoboken, NJ, USA: John Wiley & Sons, Inc., Mar. 2003.

[18] J. Krim, "Friction and energy dissipation mechanisms in adsorbed molecules and molecularly thin films," *Adv. Phys.*, vol. 61, pp. 155–323, June 2012.

[19] M. Cieplak, E. D. Smith, and M. O. Robbins, "Molecular Origins of Friction: The Force on Adsorbed Layers," *Sci.*, vol. 265, pp. 1209–1212, Aug. 1994.

[20] M. S. Tomassone, J. B. Sokoloff, A. Widom, and J. Krim, "Dominance of Phonon Friction for a Xenon Film on a Silver (111) Surface," *Phys. Rev. Lett.*, vol. 79, pp. 4798–4801, Dec. 1997.

[21] M. S. Tomassone and A. Widom, "Electronic friction forces on molecules moving near metals," *Phys. Rev. B*, vol. 56, pp. 4938–4943, Aug. 1997.

[22] T. A. L. Burgo, C. A. Silva, L. B. S. Balestrin, and F. Galembeck, "Friction coefficient dependence on electrostatic tribocharging," *Sci. Rep.*, vol. 3, p. 2384, Dec. 2013.

[23] G. A. Bird, "Molecular gas dynamics," *NASA STI/Recon Tech. Rep. A*, vol. 76, p. 40225, 1976.

[24] D. A. Lockerby, J. M. Reese, and M. A. Gallis, "The usefulness of higher-order constitutive relations for describing the Knudsen layer," *Phys. Fluids*, vol. 17, no. 10, p. 100609, 2005.

[25] T. Qian, X.-P. Wang, and P. Sheng, "Molecular scale contact line hydrodynamics of immiscible flows," *Phys. Rev. E*, vol. 68, p. 016306, July 2003.

[26] P. A. Thompson and M. O. Robbins, "Simulations of contact-line motion: Slip and the dynamic contact angle," *Phys. Rev. Lett.*, vol. 63, pp. 766–769, Aug. 1989.

[27] E. Bertrand, T. D. Blake, and J. D. Coninck, "Influence of solid–liquid interactions on dynamic wetting: A molecular dynamics study," *J. Phys.: Condens. Matter*, vol. 21, p. 464124, Nov. 2009.

[28] U. Lācis, P. Johansson, T. Fullana, B. Hess, G. Amberg, S. Bagheri, and S. Zaleski, "Steady moving contact line of water over a no-slip substrate: Challenges in benchmarking phase-field and volume-of-fluid methods against molecular dynamics simulations," *Eur. Phys. J. Spec. Top.*, vol. 229, pp. 1897–1921, Sept. 2020.

[29] A. V. Lukyanov and A. E. Likhtman, "Relaxation of Surface Tension in the Liquid–Solid Interfaces of Lennard-Jones Liquids," *Langmuir*, vol. 29, pp. 13996–14000, Nov. 2013.

[30] J. S. Rowlinson and B. Widom, *Molecular Theory of Capillarity*. Mineola, New York: Dover Publications, Inc., 2002.

[31] F. P. Buff, R. A. Lovett, and F. H. Stillinger Jr, "Interfacial density profile for fluids in the critical region," *Phys. Rev. Lett.*, vol. 15, no. 15, p. 621, 1965.

[32] E. Chacón and P. Tarazona, "Intrinsic profiles beyond the capillary wave theory: A Monte Carlo study," *Phys. Rev. Lett.*, vol. 91, no. 16, p. 166103, 2003.

[33] A. Werner, F. Schmid, M. Müller, and K. Binder, "Anomalous size-dependence of interfacial profiles between coexisting phases of polymer mixtures in thin-film geometry: A Monte Carlo simulation," *J. Chem. Phys.*, vol. 107, pp. 8175–8188, Nov. 1997.

[34] A. Werner, F. Schmid, M. Müller, and K. Binder, ""Intrinsic" profiles and capillary waves at homopolymer interfaces: A Monte Carlo study," *Phys. Rev. E*, vol. 59, pp. 728–738, Jan. 1999.

[35] M. Jorge and M. N. D. Cordeiro, "Intrinsic structure and dynamics of the water/nitrobenzene interface," *The J. Phys. Chem. C*, vol. 111, no. 47, pp. 17612–17626, 2007.

[36] L. B. Pártay, G. Hantal, P. Jedlovszky, Á. Vincze, and G. Horvai, "A new method for determining the interfacial molecules and characterizing the surface roughness in computer simulations. Application to the liquid–vapor interface of water," *J. Comput. Chem.*, vol. 29, no. 6, pp. 945–956, 2008.

[37] A. P. Willard and D. Chandler, "Instantaneous Liquid Interfaces," *J. Phys. Chem. B*, vol. 114, pp. 1954–1958, Feb. 2010.

[38] M. Sega, S. S. Kantorovich, P. Jedlovszky, and M. Jorge, "The generalized identification of truly interfacial molecules (ITIM) algorithm for nonplanar interfaces," *J. Chem. Phys.*, vol. 138, p. 044110, Jan. 2013.

[39] M. Sega, M. Sbragaglia, L. Biferale, and S. Succi, "Regularization of the slip length divergence in water nanoflows by inhomogeneities at the Angstrom scale," *Soft Matter*, vol. 9, no. 35, pp. 8526–8531, 2013.

[40] C.-H. Chung and S. Yip, "Generalized Hydrodynamics and Time Correlation Functions," *Phys. Rev.*, vol. 182, pp. 323–339, June 1969.

[41] N. K. Ailawadi, A. Rahman, and R. Zwanzig, "Generalized Hydrodynamics and Analysis of Current Correlation Functions," *Phys. Rev. A*, vol. 4, pp. 1616–1625, Oct. 1971.

[42] R. Borcia, I. D. Borcia, and M. Bestehorn, "Drops on an arbitrarily wetting substrate: A phase field description," *Phys. Rev. E*, vol. 78, no. 6, p. 066307, 2008.

[43] F. Montefuscolo, F. S. Sousa, and G. C. Buscaglia, "High-order ALE schemes for incompressible capillary flows," *J. Comput. Phys.*, vol. 278, 2014.

[44] U. Thiele, K. Neuffer, M. Bestehorn, Y. Pomeau, and M. G. Velarde, "Sliding drops on an inclined plane," *Colloids Surfaces A: Physicochem. Eng. Aspects*, vol. 206, no. 1-3, pp. 87–104, 2002.

[45] L. Schwartz, D. Roux, and J. Cooper-White, "On the shapes of droplets that are sliding on a vertical wall," *Phys. D: Nonlinear Phenom.*, vol. 209, no. 1-4, pp. 236–244, 2005.

[46] J. Snoeijer, N. Le Grand-Piteira, L. Limat, H. A. Stone, and J. Eggers, "Cornered drops and rivulets," *Phys. Fluids*, vol. 19, no. 4, p. 042104, 2007.

[47] W. Ren and W. E, "Boundary conditions for the moving contact line problem," *Phys. Fluids*, vol. 19, p. 022101, Feb. 2007.

[48] X. Xu, Y. Di, and M. Doi, "Variational method for contact line problems in sliding liquids," *Phys. Fluids*, vol. 28, p. 087101, 2016.

[49] D. Peschka, "Variational approach to contact line dynamics for thin films," *Phys. Fluids*, vol. 30, 2018.

[50] M. J. Abraham, T. Murtola, R. Schulz, S. Páll, J. C. Smith, B. Hess, and E. Lindahl, "GROMACS: High performance molecular simulations through multi-level parallelism from laptops to supercomputers," *SoftwareX*, vol. 1–2, pp. 19–25, Sept. 2015.

[51] H. J. C. Berendsen, J. R. Grigera, and T. P. Straatsma, "The missing term in effective pair potentials," *J. Phys. Chem.*, vol. 91, pp. 6269–6271, Nov. 1987.

[52] S. Nosé, "A molecular dynamics method for simulations in the canonical ensemble," *Mol. Phys.*, vol. 52, no. 2, pp. 255–268, 1984.

[53] W. G. Hoover, "Canonical dynamics: Equilibrium phase-space distributions," *Phys. Rev. A*, vol. 31, no. 3, p. 1695, 1985.

[54] M. Sega and P. Jedlovszky, "The impact of tensorial temperature on equilibrium thermodynamics," *Phys. Chem. Chem. Phys.*, vol. 20, no. 25, pp. 16910–16912, 2018.

[55] S. Miyamoto and P. A. Kollman, "Settle: An analytical version of the SHAKE and RATTLE algorithm for rigid water models," *J. Comput. Chem.*, vol. 13, no. 8, pp. 952–962, 1992.

[56] U. Essmann, L. Perera, M. L. Berkowitz, T. Darden, H. Lee, and L. G. Pedersen, "A smooth particle mesh Ewald method," *J. Chem. Phys.*, vol. 103, pp. 8577–8593, Nov. 1995.

[57] N. Michaud-Agrawal, E. J. Denning, T. B. Woolf, and O. Beckstein, "MDAnalysis: A toolkit for the analysis of molecular dynamics simulations," *J. Comput. Chem.*, vol. 32, no. 10, pp. 2319–2327, 2011.

[58] M. Sega, G. Hantal, B. Fábián, and P. Jedlovszky, "Pytim: A python package for the interfacial analysis of molecular simulations," *J. Comput. Chem.*, vol. 39, pp. 2118–2125, Sept. 2018.

[59] I. Shvab and R. J. Sadus, "Intermolecular potentials and the accurate prediction of the thermodynamic properties of water," *The J. Chem. Phys.*, vol. 139, p. 194505, Nov. 2013.

[60] M. Sega and C. Dellago, "Long-Range Dispersion Effects on the Water/Vapor Interface Simulated Using the Most Common Models," *J. Phys. Chem. B*, vol. 121, pp. 3798–3803, Apr. 2017.